

Minimally Redundant 2-D Array Designs for 3-D Medical Ultrasound Imaging

Mustafa Karaman*, *Member, IEEE*, Ira O. Wygant, *Student Member, IEEE*, Ömer Oralkan, *Member, IEEE*, and Butrus T. Khuri-Yakub, *Fellow, IEEE*

Abstract—In real-time ultrasonic 3-D imaging, in addition to difficulties in fabricating and interconnecting 2-D transducer arrays with hundreds of elements, there are also challenges in acquiring and processing data from a large number of ultrasound channels. The coarray (spatial convolution of the transmit and receive arrays) can be used to find efficient array designs that capture all of the spatial frequency content (a transmit–receive element combination corresponds to a spatial frequency) with a reduced number of active channels and firing events. Eliminating the redundancies in the transmit–receive element combinations and firing events reduces the overall system complexity and improves the frame rate. Here we explore four reduced redundancy 2-D array configurations for miniature 3-D ultrasonic imaging systems. Our approach is based on 1) coarray design with reduced redundancy using different subsets of linear arrays constituting the 2-D transducer array, and 2) 3-D scanning using fan-beams (narrow in one dimension and broad in the other dimension) generated by the transmit linear arrays. We form the overall array response through coherent summation of the individual responses of each transmit–receive array pairs. We present theoretical and simulated point spread functions of the array configurations along with quantitative comparison in terms of the front-end complexity and image quality.

Index Terms—Beamforming, biomedical ultrasonics, image reconstruction, phased arrays, ultrasonic imaging.

I. INTRODUCTION

REAL-TIME 3-D ultrasound imaging extends the frontiers of traditional diagnostic ultrasound by providing a full view of internal tissue structures along with flow information. Volumetric ultrasound with miniature devices such as endoscopes or intracavitary probes provides unique opportunities for guiding surgeries or minimally invasive therapeutic procedures. The historical progress, the state-of-art and clinical utility of 3-D ultrasound imaging has been extensively reviewed in [1]–[6]. Research studies on 3-D ultrasound imaging concentrate on transducer design, array signal processing, and image visualization. Volumetric imaging systems employ 2-D transducer arrays that consist of hundreds of elements, and necessitate data acquisition probes with integrated front-end elec-

tronics and reduced number of electrical connections [2]–[4]. For real-time 3-D imaging, in addition to difficulties in fabricating and interconnecting 2-D transducer arrays [8], [9], there are also challenges in acquiring and processing data from a large number of ultrasound channels [10], [11]. Conventional phased array (CPA) imaging utilizes all of the array elements in transmit and receive. It provides the best possible image quality for a given array, and hence is considered the gold-standard. For large arrays and especially for 2-D arrays that consist of thousands of elements, CPA is difficult to implement in hardware because of the large number of active elements. Moreover, large numbers of scan lines in volumetric imaging result in reduced frame rates and/or view angles due to the finite speed of sound. The real-time imaging is constrained as

$$\left(\frac{\# \text{ of Frames}}{\text{Second}}\right) \times \left(\frac{\# \text{ of Firings}}{\text{Frame}}\right) \times \left(\frac{2 \times \text{Image Depth}}{\text{Speed of Sound}}\right) \leq 1. \quad (1)$$

For example, a 64×64 -element CPA system can produce a single 90° , 15-cm-deep pyramidal volume image in 1.6 s. To reduce the front-end complexity and improve data acquisition speed, various array processing techniques based on synthetic aperture [12]–[24], sparse arrays [25]–[30], parallel beamforming [31]–[36], rectilinear scanning [29], [37]–[39], phased subarray processing [40]–[42], coded excitation [43]–[46], micro beamformers [7], [47], [48], configurable arrays [7], [49], and separate transmit and receive arrays [50]–[52], [58], [53] have been proposed.

In classical synthetic aperture (CSA) imaging a single active element is stepped across a large transducer array at successive data acquisition steps by channel multiplexing. The image is reconstructed through synthetic beamforming using the collected A-scan data. CSA suffers from low signal-to-noise ratio (SNR), poor contrast resolution and artifacts due to tissue and transducer motion. The SNR performance can be improved by transmitting from multiple neighboring elements with defocusing phases to form a powerful, virtual element [15], [20], [22]. To improve the contrast resolution, one can use a small active receive subarray with a slight increase in the front-end complexity [15], [23]. Susceptibility of CSA imaging to tissue and transducer motion can be reduced by various motion estimation and compensation techniques [12], [18], [21]. In 3-D CSA imaging, the large number of firing events (data acquisition steps) limits the frame rate and efficiency of motion compensation.

Sparse array processing is based on aperture undersampling using periodic or random sampling, and has been used widely to simplify the front-end by reducing the active channel count.

Manuscript received September 19, 2008; revised December 05, 2008. First published December 8, 2008; current version published June 24, 2009. This work was supported in part by the National Institutes of Health under Grant 99059, in part by TUBITAK of Turkey under Grant 106M333, and in part by Işık University under Grant BAP-05B301. *Asterisk indicates corresponding author.*

*M. Karaman is with the Department of Electronics Engineering, Işık University, 34980 Istanbul, Turkey (e-mail: karaman@isikun.edu.tr).

I. O. Wygant, Ö. Oralkan, and B. T. Khuri-Yakub are with the Ginzton Laboratory, Stanford University, Stanford, CA 94305 USA (e-mail: iwygant@stanford.edu; ooralkan@stanford.edu; khuri-yakub@stanford.edu).

Digital Object Identifier 10.1109/TMI.2008.2010936

In general sparse array design aims to achieve a desired beam pattern using a subset of array elements through optimization techniques. Various recent studies have demonstrated 2-D sparse arrays for 3-D imaging [25]–[30]. Periodic sparse arrays suffer from grating lobe artifacts, whereas random sparse arrays distribute the grating lobe energy over the side lobes, resulting in increased average side lobe levels. The sparse array design seems to be an efficient solution if the contrast resolution requirement in a particular application can be satisfied by the given active element count. In addition to challenges in 2-D sparse array optimization to achieve an acceptable image quality with a tolerable active channel count, there are also difficulties in real-time volumetric scanning due to the large number of firings.

Parallel beamforming has been proposed to meet real-time frame rate requirements in volumetric imaging [31]–[36]. In this approach, a transmit beam with a wide main lobe is produced by using a subarray, and a number of parallel, narrow receive beams spanning the main lobe of the transmit beam are formed by using a large receive array. Alternatively, multiple simultaneous narrow transmit beams at different angles can be produced by using subarrays, or a periodically undersampled array, or by firing superimposed steered beams from a large array. As a result, the number of firings is scaled down by the number of parallel beams at the expense of reduced beam quality. Rectilinear scanning extends the principle of linear scanning to 3-D imaging. In rectilinear scanning, each linear array (row or column) on a 2-D array is used to form a plane beam, and image lines on that plane are reconstructed by parallel beamforming using a 2-D receive array [24], [30]–[34]. Use of separate transmit and receive arrays in data acquisition simplifies the front-end hardware complexity, and enables synthesis of different transmit–receive array configurations. Various recent studies have used this approach for volumetric scanning with different array shapes [24], [30]–[34], [51], [52], [58], [53].

The phased subarray approach combines the principles of phased array and synthetic aperture imaging to reduce the system complexity by decreasing the active channel count [40]–[42]. Similar to CPA processing, the low-resolution subarray images are generated by scanning the space with a small beam count proportional to the subarray size. These low-resolution images are laterally upsampled, interpolated, weighted, and coherently summed to form the final high-resolution image. For narrowband systems the subarray-dependent 1-D interpolation filters can perform well [40], whereas wideband imaging requires 2-D filters for beam interpolation [41], [42].

For nearly any type of beamforming, coded excitation can be used to boost the SNR and the penetration depth as well as the frame rate [43]–[46]. To improve the frame rate, the basic idea is to generate non-interfering wavefronts in the image space by firing uncorrelated coded signals from array elements. Consequently, echo signals can be decoded for simultaneous reconstruction of multiple scan lines. Generation of efficient uncorrelated codes with reasonable lengths and efficient decoding schemes to minimize the degradation in axial resolution are major difficulties to utilize the promising benefits of coded excitation approach for increasing frame rate.

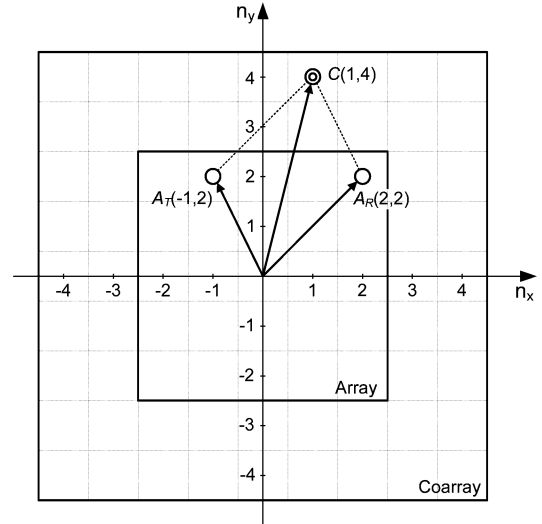


Fig. 1. Physical array and coarray kernels, where each transmit and receive element combination produces a coarray element.

Integration of some of the electronics with the transducer array enables miniaturization of the front-end and funneling the electrical connections of a 2-D array consisting of thousands of elements into a reduced number of channels. This allows realization of configurable arrays by using switching matrix circuits and subarray micro-beamformers [7], [47]–[49]. These approaches are very promising for 3-D and portable 2-D imaging applications, where the miniaturization of the array front-end is necessary. Three-dimensional state-of-the-art systems based on the subarray micro-beamforming are already available [2], [4]–[6]. Such systems employing fully sampled piezoelectric matrix arrays (consisting of nearly 3000 elements) and using only 128 channels of a standard scanner, can generate narrow volume images in real time, or wider volume images by time-gating (4–8 cardiac cycles) [5], [6]. More recently, research studies on CMUT-based imaging systems have also demonstrated that front-end circuits can be integrated with CMUT arrays using flip-chip bonding techniques [9], [49], [54], [55] and monolithic silicon processing [50]–[52], [58].

II. TWO-DIMENSIONAL ARRAY PROCESSING TECHNIQUES

A. Approach

The image quality of a pulse-echo array system can be quantified by the coarray function (also called the effective aperture) which corresponds to the convolution of the transmit, and receive arrays [10], [15], [16], [19], [41], [56]

$$C(n_x, n_y) = A_T(n_x, n_y) \otimes A_R(n_x, n_y) \quad (2)$$

here the indexes n_x and n_y are the discrete variables representing locations of 2-D array elements (Fig. 1); $A_T(\cdot)$, $A_R(\cdot)$, and $C(\cdot)$ are the 2-D transmit array, receive array, and coarray functions, respectively. The far-field, continuous wave

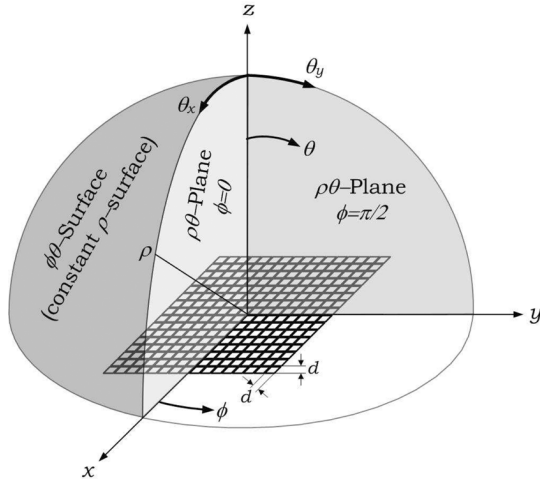


Fig. 2. Reference geometry used for the theoretical and simulated PSFs.

point spread function (PSF) of the array imaging system can be approximated by the Fourier transform of the coarray

$$H(\alpha, \beta) = \mathbb{F}\{C(n_x, n_y)\} = \mathbb{F}\{A_T(n_x, n_y)\} \times \mathbb{F}\{A_R(n_x, n_y)\},$$

$$(n_x, n_y) \xleftrightarrow{\mathbb{F}} (2\alpha, 2\beta); \alpha = \frac{\pi d}{\lambda} \sin \theta_x; \beta = \frac{\pi d}{\lambda} \sin \theta_y. \quad (3)$$

Here λ is the wavelength, d is the inter-element distance, and θ_x and θ_y , respectively, are the angles in azimuth and elevation directions (Fig. 2). Note that the Fourier transform relation is between the discrete aperture space and the continuous image space represented by the pairs of variables, (n_x, n_y) and $(2\alpha, 2\beta)$, respectively. Each combination of a transmit element and a receive element produces a coarray element whose spatial location corresponds to the sum of position vectors of the transmit and receive elements (Fig. 1)

$$\underbrace{(n_{x,C}, n_{y,C})}_{\text{Coarray Element}} = \underbrace{(n_{x,T}, n_{y,T})}_{\text{Transmit Element}} + \underbrace{(n_{x,R}, n_{y,R})}_{\text{Receive Element}}$$

$$= \underbrace{((n_{x,T} + n_{x,R}), (n_{y,T} + n_{y,R}))}_{\text{Coarray Element}}. \quad (4)$$

Consequently, different combinations of transmit and receive elements in the convolution operation may contribute to the same coarray elements. Considering the Fourier relation between the aperture and image spaces, each sample of the coarray corresponds to a spatial frequency. The multiple combinations contributing to the same coarray element actually corresponds to the redundancy in the spatial frequency. In array design, the idea is to form a coarray which is minimally redundant in spatial frequency content; that is, a coarray that captures all of the spatial frequency content with a minimum number of transmit/receive element pairs (each element of a nonredundant coarray involves only a single transmit–receive element pair).

Volumetric scanning with 2-D arrays requires excessive number of scan lines (firings). In pulse-echo imaging using an $N \times N$ element array ($N \gg 1$) with an inter-element spacing

of d , the number of firings (scan lines) to form a pyramidal volumetric frame with an angle of $(\theta_x \times \theta_y)$ is given by

$$B_x \times B_y \geq \left(\frac{4Nd}{\lambda} \sin \left(\frac{\theta_x}{2} \right) \right) \times \left(\frac{4Nd}{\lambda} \sin \left(\frac{\theta_y}{2} \right) \right). \quad (5)$$

Note that the beam count in each dimension must be scaled by 2 when one-way response is considered. To produce a 90° volumetric frame using pulse-echo CPA imaging with $d = \lambda/2$, the minimum number of firings is $(\sqrt{2} \times N) \times (\sqrt{2}N)$. On the other hand, the frame rate is inversely proportional to the array size and/or the number of signal firing/receiving steps as indicated by (1). In array processing, the firing count must also be kept small enough to meet real-time imaging requirements. Our approach to explore array processing for miniature volumetric imaging systems is based on 1) coarray design with reduced redundancy using different subsets of linear arrays constituting the 2-D transducer array, and 2) volumetric scanning using fan-beams (narrow in one dimension and broad in the other dimension) generated by the transmit linear arrays.

B. Two-Dimensional Array Configurations

Here we describe four array configurations involving reduced or minimum spatial frequency redundancy. Each design explores a different tradeoff between the image quality and the front-end complexity. For comparison, we consider CPA and CSA as the reference methods providing the best image quality and the simplest front-end, respectively. Using the continuous wave, paraxial and far-field approximations, the two-way PSF of CPA with an $N \times N$ square array, $H_{\text{CPA}}(\alpha, \beta)$, can be expressed by

$$H_{\text{CPA}}(\alpha, \beta) \propto \left(\frac{\sin(\alpha N)}{\sin(\alpha)} \times \frac{\sin(\beta N)}{\sin(\beta)} \right) \times \left(\frac{\sin(\alpha N)}{\sin(\alpha)} \times \frac{\sin(\beta N)}{\sin(\beta)} \right) \quad (6)$$

where $\alpha = (\pi d/\lambda) \sin(\theta_x)$, $\beta = (\pi d/\lambda) \sin(\theta_y)$, and θ_x and θ_y , respectively, are the angles in azimuth and elevation directions (Fig. 2) [31]. Similarly, PSF of the CSA is approximated by

$$H_{\text{CSA}}(\alpha, \beta) \propto \left(\frac{\sin(2\alpha N)}{\sin(2\alpha)} \times \frac{\sin(2\beta N)}{\sin(2\beta)} \right). \quad (7)$$

Note that the first and second terms in the PSF expressions given above and in the following subsections, correspond to the transmit and receive responses of the array, respectively. All analytical PSF expressions are normalized by the two-way response of a single array element given by

$$h_e(\alpha, \beta) \propto \left(\frac{\sin(\alpha)}{\alpha} \times \frac{\sin(\beta)}{\beta} \right) \times \left(\frac{\sin(\alpha)}{\alpha} \times \frac{\sin(\beta)}{\beta} \right). \quad (8)$$

For the sake of simplicity in derivation, the analytical PSFs of the four array designs presented below are approximated by assuming that the common elements are used both in transmit and in receive. The transmit, receive and coarray functions of the array configurations considered here are illustrated in Fig. 3. We also computed the far-field, continuous-wave PSFs based on the approximate analytical expressions including the two-way response of a single element given in (8) with $d = \lambda/2$. The

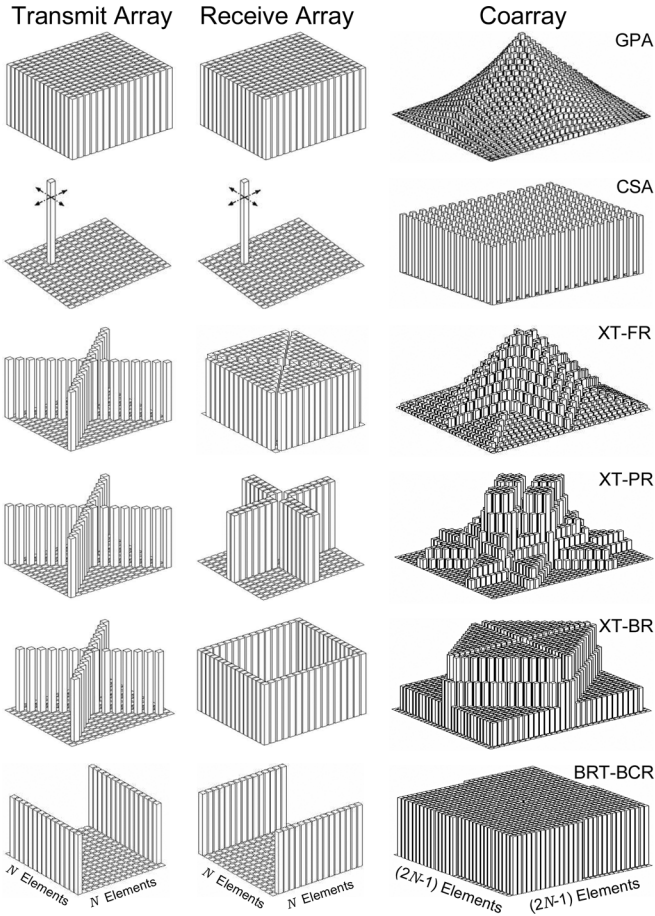


Fig. 3. Schematics of the transmit, receive and coarray functions for different array configurations. Each bar in the array functions represents an element's amplitude. The amplitude of each array function (vertical dimension) is normalized to unity. The transmit and receive arrays are configured over a 16×16 -element square array, and the resulting coarray size is 31×31 . The stepping the active element in CSA over the array in successive firings is indicated by the arrows.

results are presented in Fig. 4, where each PSF distribution (on a constant ρ surface) represents a C-scan as a function of the Fourier transform variables α and β [or equivalently $\sin(\theta_x)$ and $\sin(\theta_y)$].

1) *X-Shaped Transmitter and Full Receiver (XT-FR)*: In this configuration, the transmit array is a cross-shaped aperture formed by the two diagonals of the 2-D transducer array, while the entire array is utilized in receive (see Fig. 3). Assuming that the transmit elements are also used in receive, the PSF of this configuration, can be approximated by

$$H_{\text{XT-FR}}(\alpha, \beta) \propto \left(\frac{\sin((\alpha - \beta)N)}{\sin(\alpha - \beta)} + \frac{\sin((\alpha + \beta)N)}{\sin(\alpha + \beta)} \right) \times \left(\frac{\sin(\alpha N)}{\sin(\alpha)} \times \frac{\sin(\beta N)}{\sin(\beta)} \right). \quad (9)$$

Note that the first term corresponds to the sum of responses of two diagonal linear arrays, whereas the second term is one-way response of a square array. The computed PSF of XT-FR is displayed in Fig. 4.

2) *X-Shaped Transmitter and Plus-Shaped Receiver (XT-PR)*: In this configuration the transmit array is a cross-shaped aperture formed by two perpendicular linear

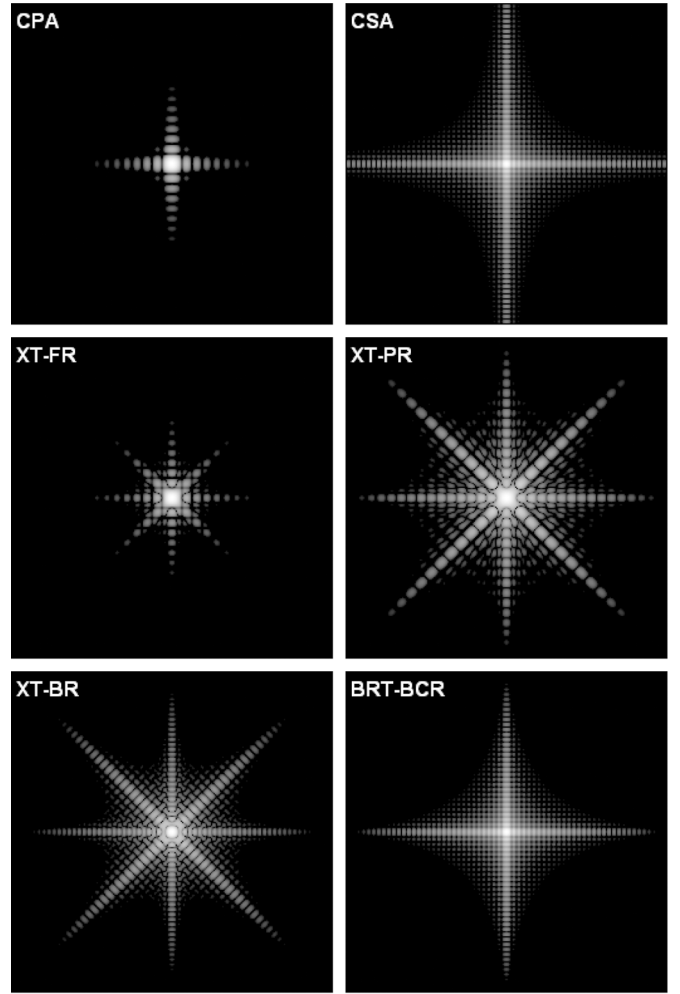


Fig. 4. Computed theoretical (far-field, continuous-wave) PSFs. Each PSF represents a C-scan over a constant- ρ surface. The horizontal axis is $(-\pi/2 \leq \alpha \leq \pi/2)$ (equivalently $-1 \leq \sin(\theta_x) \leq 1$) and $(-\pi/2 \leq \beta \leq \pi/2)$ (equivalently $-1 \leq \sin(\theta_y) \leq 1$) and the vertical axis is $(-\pi/2 \leq \beta \leq \pi/2)$ (equivalently $-1 \leq \sin(\theta_y) \leq 1$). The display dynamic range is 50 dB.

arrays, diagonals of the 2-D transducer array, whereas the receive array is a plus-shaped aperture formed by two perpendicular linear array pairs (the vertical and horizontal arms consisting of two central rows and columns, respectively) (see Fig. 3). Considering that the central four transmit elements are also used in receive, the PSF of this configuration, can be approximated by

$$H_{\text{XT-PR}}(\alpha, \beta) \propto \left(\frac{\sin((\alpha - \beta)N)}{\sin(\alpha - \beta)} + \frac{\sin((\alpha + \beta)N)}{\sin(\alpha + \beta)} \right) \times \left(\frac{\sin(\alpha N)}{\sin(\alpha)} \cos(\alpha) + \frac{\sin(\beta N)}{\sin(\beta)} \cos(\beta) \right). \quad (10)$$

Note that the first term corresponds to the sum of the responses of two diagonal linear arrays, whereas the second term is the one-way response of the plus-shaped receive array. Also note that the cosine factors in the second term are associated with the vertical and horizontal arms consisting of two central rows and columns, respectively. The computed PSF plot of XT-FR is shown in Fig. 4.

The XT-PR configuration can be considered as an extension of the basic array configuration known as the Mills cross array, in which the transmitter and receiver are perpendicular linear arrays [24]. The XT-PR array configuration employing a plus-shaped transmitter with a single row and column and cross-shaped (diagonals) receiver has been investigated previously for phased array volumetric imaging by Smith *et al.* [31], [32]. Here we reconsider this array configuration with fan-beam scanning, and compare it with the other array configurations.

3) *X-Shape Transmitter and Boundary Receiver (XT-BR)*: This configuration employs the diagonal elements of the 2-D transducer aperture in transmit and the boundary elements in receive (see Fig. 3). We can approximate the PSF of this array design by the following expression:

$$H_{\text{XT-BR}}(\alpha, \beta) \propto \left(\frac{\sin((\alpha - \beta)N)}{\sin(\alpha - \beta)} + \frac{\sin((\alpha + \beta)N)}{\sin(\alpha + \beta)} \right) \times \left(\frac{\sin(\alpha N)}{\sin(\alpha)} \cos(\beta N) + \frac{\sin(\beta N)}{\sin(\beta)} \cos(\alpha N) \right). \quad (11)$$

Here the first term is the same as that of (9) and (10), and the second term is the one-way response of a square boundary array, approximated by the sum of the responses of two horizontal and two vertical linear arrays (the corner elements are considered as the common elements). The computed PSF of XT-BR is given in Fig. 4. A rectangular boundary array with different weighting schemes used both as the transmitter and receiver has been investigated previously by Kozick and Kassam [13]. The XT-BR explored here has two distinctions from the earlier configurations: it employs an X-shaped array in transmit and a boundary array in receive, and involves fan-beam processing for volumetric scanning.

4) *Boundary-Rows Transmitter and Boundary-Columns Receiver (BRT-BCR)*: This array design uses two boundary rows (the outermost horizontal linear arrays) in transmit and two boundary columns (the outermost vertical linear arrays) in receive, and produces a uniform coarray with no redundant spatial frequency (Fig. 3). The approximate PSF of this scheme corresponds to multiplication of the summed responses in the second term of (11)

$$H_{\text{BRT-BCR}}(\alpha, \beta) \propto \left(\frac{\sin(\alpha N)}{\sin(\alpha)} \cos(\beta N) \right) \times \left(\frac{\sin(\beta N)}{\sin(\beta)} \cos(\alpha N) \right). \quad (12)$$

The computed, continuous-wave, far-field PSF of BRT-BCR is shown in Fig. 4. The BRT-BCR configuration is basically an extension of a standard Mills cross array, where two spatially orthogonal N -element, linear arrays, used as the transmit and receive arrays, produce a non-redundant $(N \times N)$ -element coarray with uniform amplitude distribution [24]. The two-way PSF of the standard Mills cross array is identical to the one-way PSF of a fully populated $N \times N$ -element array; $H_{\text{Mills-Cross}}$ is equivalent to $H_{\text{BRT-BCR}}$ in (12) without the cosine terms. Considering an $N \times N$ -element transducer array, BRT-BCR uses the two N -element boundary horizontal linear arrays in transmit and the two N -element boundary vertical linear arrays in receive, and produces a coarray with size of $(2N - 1) \times (2N - 1)$.

Therefore, the size of the coarray of BRT-BCR is two times that of the Mills cross array, at the expense of doubling the transmit and receive elements or increasing the multiple firings from N active channels by 4 times. The BRT-BCR with different weighting schemes has been investigated previously by Kozick and Kassam [13]. Here we reconsider this array configuration to improve its frame rate by using the fan-beam scanning, and compare it with the other array configurations.

C. Fan-Beam Processing

For real-time volumetric scanning, we use transmit fan-beams generated by the linear arrays to reduce the firing count. A subset of elements on a 2-D transducer array chosen along a line, forming a “linear array,” produces a fan-shaped beam (fan-beam), narrow in one dimension and broad in the other. The narrow beam width on the scanning plane is determined by the length of the linear array, while the wide beam width orthogonal to the scanning plane is determined by the element pitch. In volumetric scanning, we insonify a plane of the volumetric field by a fan-beam, and then we reconstruct the image pixels on that plane through parallel receive beam-forming. We repeat this process for each plane of the volumetric field using steered fan-beams. The fan-beam processing can be implemented using any of the array configurations presented here. As an example, fan-beam scanning using the XT-BR array configuration is illustrated in Fig. 5(a). Note that the chosen transmit 2-D subarray array must be decomposable into linear arrays, and data acquisition must be repeated for each transmit linear array. The data from these acquisitions are added coherently to form the overall image. This process is illustrated in Fig. 5(b) for the XT-BR configuration.

The fan-beam pattern is identical to the one-way response of the N -element active linear array

$$h_{\text{FB}}(\alpha, \beta) \propto \frac{\sin(\beta N)}{\sin(\beta)} \times \left(\frac{\sin(\alpha)}{\alpha} \times \frac{\sin(\beta)}{\beta} \right) \quad (13)$$

where the second term is the one-way response of a single element. For illustration, the simulated wide-band transmit beam patterns of three different linear array configurations on a 2-D array are presented in Fig. 6, where the parameters given in Table I were used in the simulations. Different than a one-element wide horizontal or vertical linear array [Fig. 5(a)], the one-element wide diagonal linear array produces grating lobes in its one-way beam pattern as seen in Fig. 6(b). These grating lobes are caused by the aperture undersampling since the inter-element distance along the diagonal linear array on a 2-D array with $\lambda/2$ -element spacing, is $\sqrt{2}\lambda/2$. These grating lobes can be suppressed to an acceptable level by the receiver array as demonstrated by the simulations in the next section. Note that a multi-element wide diagonal linear array (whose interelement-spacing becomes $\sqrt{2}\lambda/4$) can produce a fan-beam without any grating lobes at the expense of reducing beam angle. As an example, the response of a three-element wide diagonal array is shown in Fig. 6(c). This drawback can be handled by defocused excitation of the multi-element wide diagonal linear arrays [15], [51]. In the rest of this paper we consider only the one-element

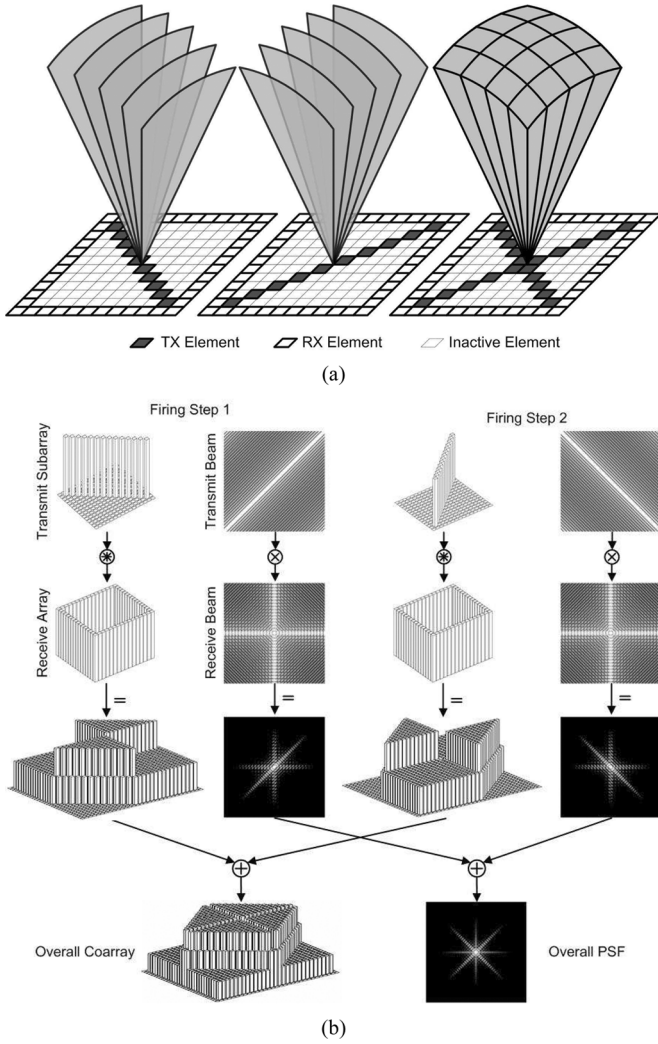


Fig. 5. Illustration of coherent fan-beam processing using XT-BR array configuration: (a) a schematic of volumetric scanning and (b) coherent processing.

wide transmit linear arrays in the simulation and comparison of the array configurations.

In fan-beam processing using an $N \times N$ element array ($N \gg 1$) with an inter-element spacing of d , the number of firings to form a pyramidal volume with an angle of $(\theta_P \times \theta_P)$ is

$$B_P \geq K \left(\frac{2Nd}{\lambda} \sin \left(\frac{\theta_P}{2} \right) \right) \quad (14)$$

where K denotes the number of linear arrays forming the transmit array. Note that this is achieved by performing parallel receive beamforming to compute the image pixels on the plane insonified by the transmit fan-beam. To produce a 90° volumetric frame with $d = \lambda/2$, the minimum number of firings is $K \times (\sqrt{2} \times N)$. In other words fan-beam processing reduces the firing count from $O(N^2)$ to $O(KN)$.

Fan-beam processing involves K successive firings for the reconstruction of pixels on a cross-sectional image plane, and hence increases the susceptibility to tissue motion by a factor of K . For the applications targeted in this study, this drawback should be tolerable for all the four array designs, where $K = 2$.

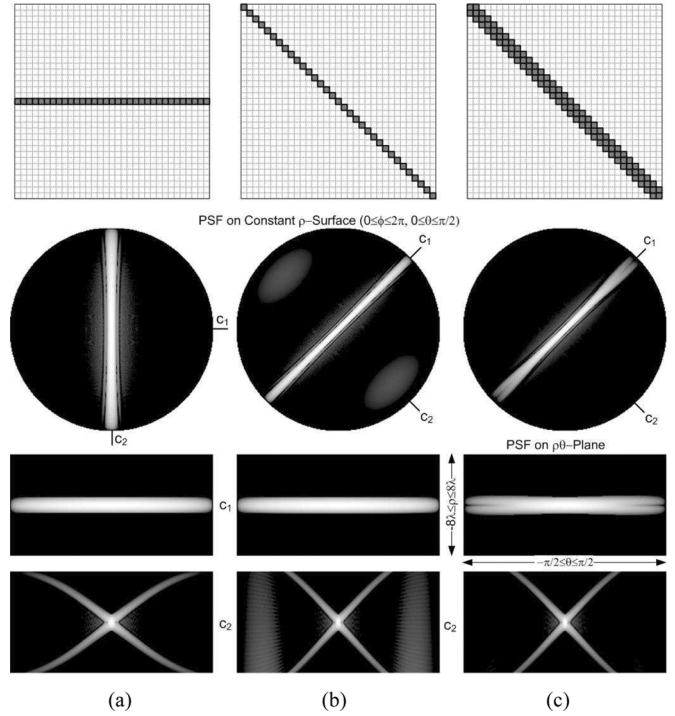


Fig. 6. Beam patterns of a horizontal (a) one-element wide diagonal (b) and three-element wide diagonal (c) linear arrays on a 32×32 -element 2-D array. The display dynamic range of PSFs is 50 dB. The PSF on the constant ρ -surface ($\phi\theta$ -surface) represents a C-scan, whereas the cross-sectional PSF on the $\rho\theta$ -plane corresponds to a B-scan.

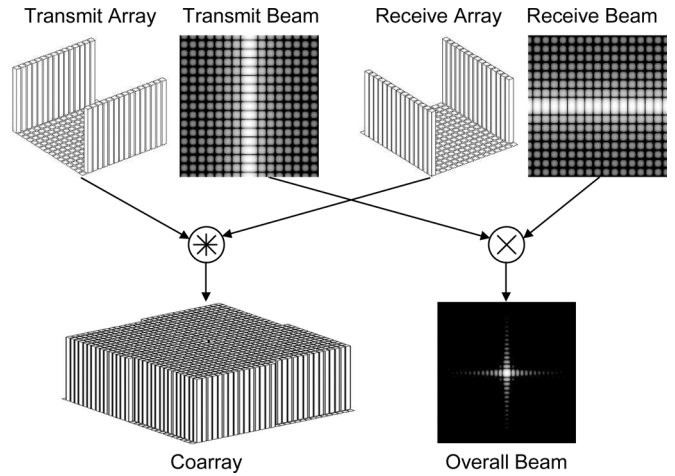


Fig. 7. Simultaneous firing from both rows of the transmit array in BRT-BCR, generates a comb-shaped fan-beam, and hence two consecutive firings are required to form a complete fan-beam to scan a plane.

In the BRT-BCR array configuration, the image volume can be scanned by firing from only one of the transmit rows at a time, or alternatively by firing both rows simultaneously. In the latter case each firing generates a comb-shaped fan-beam as illustrated in Fig. 7, and hence two consecutive firings are required to produce interleaved fan-beams.

III. PSF SIMULATIONS AND COMPARISON

To test the imaging performances of the array designs, we performed numerical PSF simulations based on the Rayleigh-

TABLE I
SIMULATION PARAMETERS

Array Size	32×32 Elements
Frequency	5 MHz
Element Pitch	150 μm ($\lambda/2$ at 5 MHz)
Excitation Pulse	Gaussian with 80% FBW
Sampling Frequency	250 MHz
Transmit Focus / Target Location	$F_{\#}$ of 4
Ultrasound Velocity	1540 m/s

Sommerfeld diffraction formulation for a point target [57]. We calculated the PSF, $H(u)$, using the following expression:

$$H(u) = \sum_n g_n \times \frac{e^{-a \cdot t_n \cdot c_0}}{t_n \cdot c_0} \times \sum_k g_k \times \frac{e^{-a \cdot t_k \cdot c_0}}{t_k \cdot c_0} \times S\left(\frac{2|u|}{c_0} - t_n - t_k - \tau_{n,T} - \tau_{k,R}\right) \quad (15)$$

where u is the 3-D vector representing the observation point, i.e., (ρ, θ, ϕ) ; the first and second summations are over the transmit and receive elements, respectively; $S(\cdot)$ is the excitation Gaussian pulse; t_n is the flight time between n th element and the point target at u_0 ; $\tau_{n,T}$ and $\tau_{k,R}$, respectively, are the transmit and receive delay times for focusing at u_T and u_R . The term g_m represents the aperture apodization and the one-way element factor (PSF of an array element). In our simulations, we used rectangular weighting (the weighting of each element is unity) to test the responses of different arrays without any aperture apodization. In computation of PSFs of the four array designs (XT-FR, XT-PR, XT-BR, and BRT-BCR), the common elements were used only in receive. For the sake of reduced computational complexity, we approximated the element factor by a cosine function, and ignored the attenuation effects, which is reasonable for testing PSF over $\theta\phi$ -surface (constant- ρ surface), and on PSF on $\rho\theta$ -plane with small axial range. As a result, the term g_m is simplified to $g_m \cong \cos((\pi d/\lambda) \cdot \sin(\varphi_m))$, where φ_m is the angle between the element's normal and the target direction ($0 \leq \varphi_m \leq \pi/2$). We implemented a custom simulation code in C and ran the simulations on a dual-core workstation computer using the simulation parameters outlined in Table I. The simulation outputs were postprocessed in Matlab for display purposes. The simulation geometry showing the array and the reference coordinate system is given in Fig. 2.

We present the first set of the simulated PSFs in Figs. 8 and 9. Here the target is located on the array normal (on-axis), and hence these PSFs represent nonsteered beam patterns. To test steered responses of the array configurations, we also performed PSF simulations for $\theta_S = 30^\circ$ and $\phi_S = 45^\circ$. These steered responses are presented in Fig. 10. For displaying 3-D PSFs, we used two orthogonal views on a constant- ρ surface ($\theta\phi$ -surface) and a $\rho\theta$ -plane (in spherical coordinates as depicted Fig. 2), which correspond to the C-scan and B-scan displays, respectively. Each image in these figures was normalized to its own maximum and log compressed to 50 dB dynamic range. For ease of comparison, the compounded, 1-D lateral cross sections of the nonsteered PSFs are also shown in Figs. 8 and 9, where the compounding was performed by averaging the 1-D

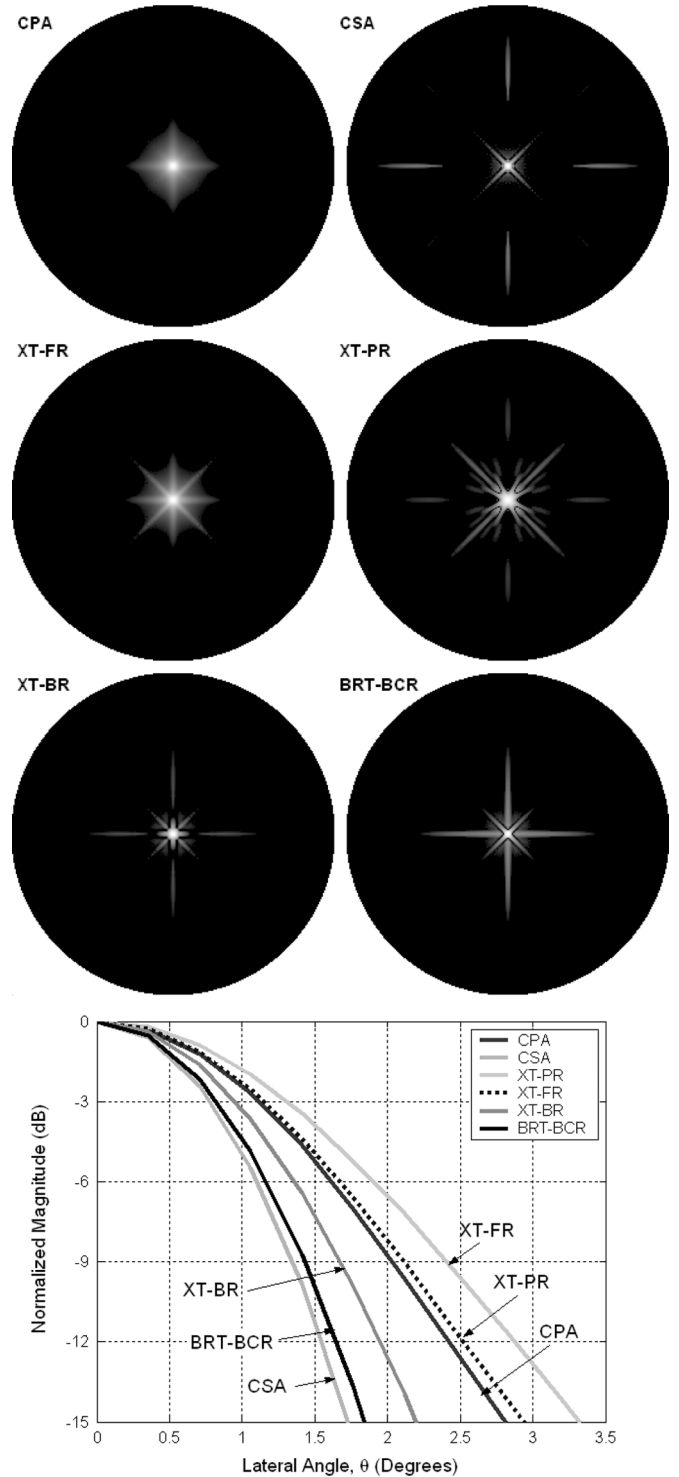


Fig. 8. Simulated PSFs of the array configurations. (a) Each PSF represents a C-scan over a constant- ρ surface ($0 \leq \theta \leq \pi/2$ and $0 \leq \phi \leq 2\pi$) with 50 dB display dynamic range. (b) Compounded, 1-D lateral cross-sections of the PSFs (showing the main lobes within -15 dB), where the 1-D cross-sections across the entire range of ϕ -extension were averaged.

cross sections across the entire ϕ -range ($0 \leq \phi \leq 2\pi$), and the ρ -range ($60\lambda \leq \rho \leq 68\lambda$), respectively. Since the PSFs vary with steering angle and do not possess full circular symmetry, a general quantitative comparison of the PSFs becomes difficult. Therefore, here we first perform a qualitative comparison of the

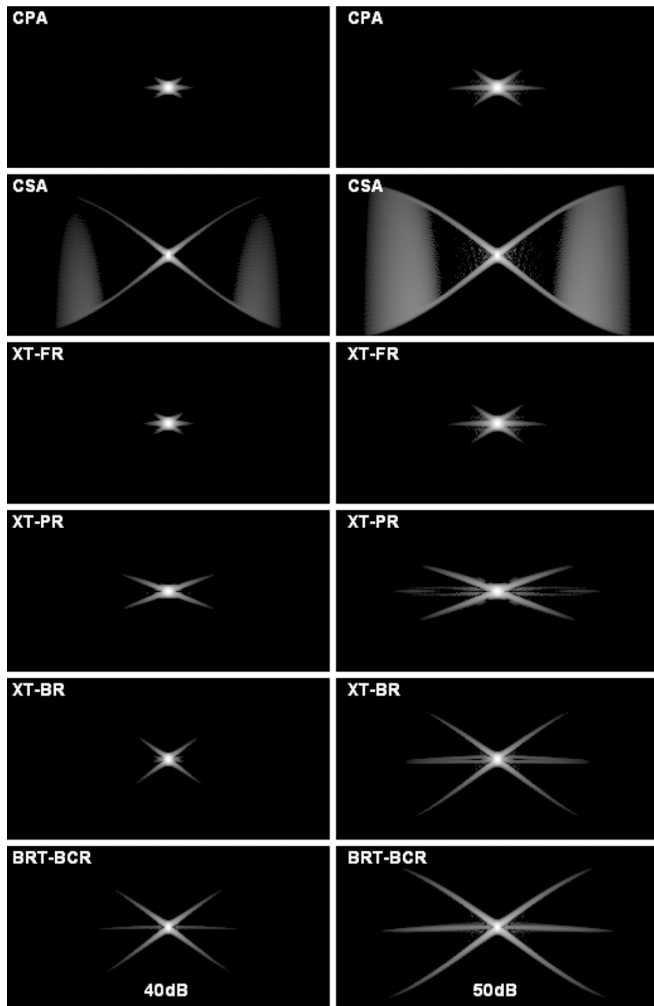


Fig. 9. Simulated PSFs of the array configurations. (a) Each PSF represents a B-scan over a $\rho\theta$ -plane (the horizontal axis: $-\pi/2 \leq \theta \leq \pi/2$; the vertical axis: $60\lambda \leq \rho \leq 68\lambda$). (b) Compounded, 1-D lateral cross-sections of the PSFs, where the 1-D cross-sections across the entire range of ρ -extension were averaged.

PSFs and then we compare the array configurations in terms of the system complexity and image quality based on quantitative parameters.

When the nonsteered and steered responses of the array configurations are examined, we observe that the PSF of CPA has

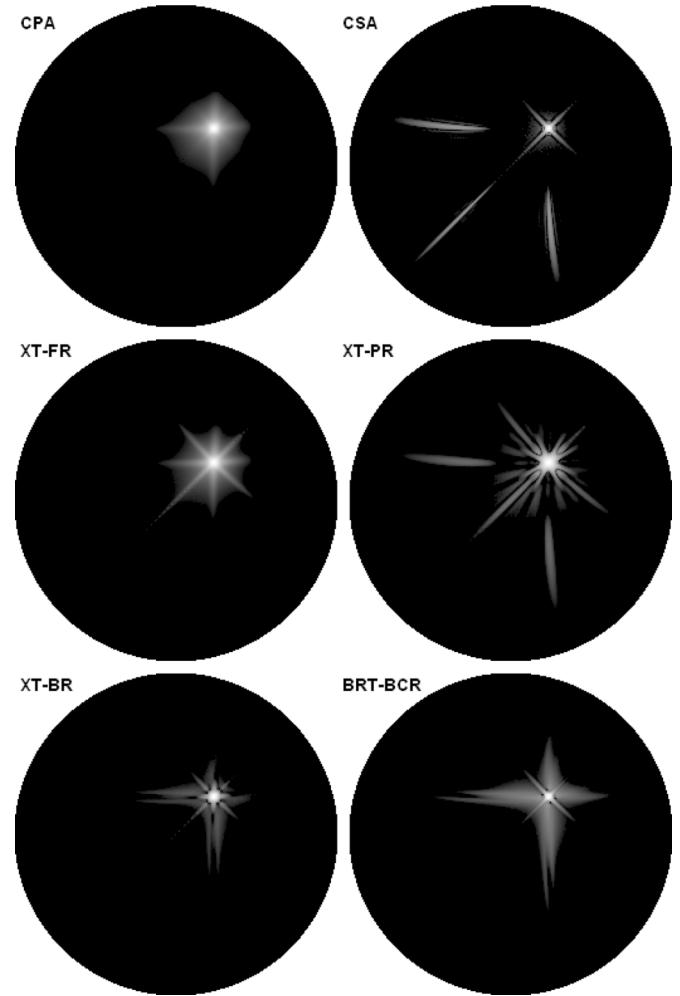


Fig. 10. Simulated PSFs steered to $\theta_s = \pi/6$ and $\phi_s = \pi/4$. Each PSF represents C-scan over the constant- ρ surface ($0 \leq \theta \leq \pi/2$ and $0 \leq \phi \leq 2\pi$) with 50-dB display dynamic range.

the lowest side lobes and wide main lobe, while the PSF of CSA has a narrow main lobe but has high side lobes and grating lobes. These observations are consistent with the approximated theoretical PSF expressions and shapes of the coarray functions. The smooth coarray function of CPA results in a wider main lobe and suppressed side lobe levels; the rectangular coarray function of CSA produces the narrow main lobe but a high side lobe level; the zeros in the coarray function produces the grating lobes. The grating lobe level, as expected, is pronounced here because of the wide bandwidth of the excitation pulse. The non-steered PSFs of CPA and XT-FR (Figs. 8 and 9) have almost identical shapes, main lobe widths, and side lobe levels. This is consistent with their similar coarray functions (Fig. 2). Comparison of their steered responses (Fig. 10) indicates that XT-FR produces slightly higher side lobe levels than CPA. In general the response of XT-FR well approximates that of CPA. While the main lobe of XT-BR is narrower than that of XT-FR, its side lobe level is higher than that of XT-FR. The XT-BR performs better than both XT-PR and BRT-BCR. The main lobe of XT-BR is narrower than that of XT-PR and comparable to that of BRT-BCR. The side lobe level of XT-BR is lower than both XT-PR and BRT-BCR. The XT-PR and BRT-BCR perform similar in terms

TABLE II
QUANTITATIVE COMPARISON OF ARRAY CONFIGURATIONS
FOR AN $N \times N$ -ELEMENT ARRAY

	CPA	CSA	XT-FR	XT-PR	XT-BR	BRT-BCR
Tx Elements	$N \times N$	$N \times N$	$2N$	$2N$	$2N$	$2N$
Rx Elements	$N \times N$	$N \times N$	$N \times N$	$4N$	$4N$	$2N$
Active Tx Channels	$N \times N$	1	N	N	N	N
Active Rx Channels	$N \times N$	1	$N \times N$	$4N$	$4N$	$2N$
Tx Beams per Frame	$2N^2$	-	$\sqrt{2}N$	$\sqrt{2}N$	$\sqrt{2}N$	$\sqrt{2}N$
Firings per Scan Line	1	-	2	2	2	2
Firings per Frame	$2N^2$	N^2	$2\sqrt{2}N$	$2\sqrt{2}N$	$2\sqrt{2}N$	$2\sqrt{2}N$
Frame Rate $\left(\times \frac{c}{2R}\right)$	$\frac{1}{2N^2}$	$\frac{1}{N^2}$	$\frac{1}{2\sqrt{2}N}$	$\frac{1}{2\sqrt{2}N}$	$\frac{1}{2\sqrt{2}N}$	$\frac{1}{2\sqrt{2}N}$
Image SNR	N^3	N	$\sqrt{2}N^2$	$2\sqrt{2}N^{3/2}$	$2\sqrt{2}N^{3/2}$	$2N^{3/2}$

of the side lobe levels, while BRT-BCR has a narrower main lobe.

Separation of transmit and receive elements (i.e., forming transmit and receive arrays with no common elements) simplifies the front-end, and allows independent optimization of transducers and front-end circuits dedicated to transmit and receive. In each of the four array designs presented here, the ratio of the number of common elements to the receive element count is $1/N$, which should be considered as a small fraction of the total. Additionally, the common elements in these array designs are not randomly distributed, but either at the center or at the boundary of the transmit and/or receive arrays. As a result, ignoring such common elements in receive, does not cause beam distortions, but may affect the beam quality slightly. To test this expectation, we also reconstructed the simulated PSFs of the four array designs (XT-FR, XT-PR, XT-BR, and BRT-BCR) with the common elements active both in transmit and receive. In 50-dB dynamic range, these PSFs, as expected, were identical to the PSFs presented in Figs. 8–10, where the common elements were active only in transmit or in receive.

For quantitative comparison, we calculated parameters quantifying the system complexity and image quality. These parameters include the active channel count, frame rate and SNR. For all array configurations, the parameters expressed in terms of the array size are shown in Table II. Here the number of firings, beam count and frame rate were calculated using the relations (1), (5), and (14). The frame rate was normalized to the round-trip flight time. The SNR gain relative to a single element's SNR is approximated as $N_T \sqrt{N_R}$ where N_T is the number of active transmit elements and N_R is the number of receive elements.

When the array configurations are compared in terms of their active channel counts quantifying the front-end complexities, both the transmit and receive front-end complexities of each of the array designs XT-PR, XT-BR, and BRT-BCR is $O(N)$ (order of N), whereas the transmit and receive front-end complexities of XT-FR are $O(N)$ and $O(N^2)$, respectively. Note that both the transmit and receive front-end complexities of CPA and CSA are $O(N^2)$ and $O(1)$, respectively. The frame rate of each of the four array configurations XT-FR, XT-PR, XT-BR, and BRT-BCR is $O(1/N)$, whereas that of CPA and CSA is

TABLE III
QUANTITATIVE COMPARISON OF ARRAY CONFIGURATIONS
FOR $N \times N = 32 \times 32$

	CPA	CSA	XT-FR	XT-PR	XT-BR	BRT-BCR
Tx Elements	1024	1024	64	64	64	64
Rx Elements	1024	1024	1024	128	128	64
Active Tx Channels	1024	1	32	32	32	32
Active Rx Channels	1024	1	1024	128	128	64
Tx Beams per Frame	2048	-	45	45	45	45
Firings per Scan Line	1	-	2	2	2	2
Firings per Frame	2048	1024	90	90	90	90
Frame Rate	12	25	285	285	285	285
Image SNR (dB)	90	30	63	54	54	51

$O(1/N^2)$. While the image SNR values of CPA and CSA are proportional to N^3 and N , respectively, the SNR of XT-FR is proportional to N^2 , and the others produce identical image SNR proportional to $N^{3/2}$.

The cost and performance parameters calculated numerically for a particular array size, 32×32 , are given in Table III. In the calculation, the speed of sound was 1540 m/s, the view angle was $90^\circ \times 90^\circ$, and the imaging depth was 30 mm. These particular settings were chosen for endoscopic ultrasound applications. For a 32×32 array, the four explored array configurations with fan-beam processing can achieve a frame rate up to 285, whereas CPA can produce 12 frames per second. The XT-FR and XT-BR, respectively, can produce 63-dB and 54-dB image SNR with a 32×32 array. Note that these SNR values are normalized by a single channel's SNR (~ 15 – 20 dB).

The amount of sound pressure generated in each firing is another critical parameter affecting the performance of array imaging. Fully populated 2-D arrays allow generation of large amount of acoustic power in transmit, and can benefit from high SNR and nonlinear acoustics applications such as critical Doppler modes and harmonic imaging. Although the ability of each of our array designs in generating sound pressure is significantly less than that of a full 2-D array, the proposed array configurations employ full 1-D linear arrays in transmit and hence can generate acoustic power sufficient for many B-mode imaging applications. To increase acoustic power from each linear array in the X-shaped transmitter and in the boundary transmit rows, it is possible to emulate a multi-element wide defocused linear array using electronic delays (Fig. 11). The transmit beam pattern of such a linear array can be controlled by the defocusing delay scheme and weighting. For 2-D imaging, it has been shown that the transmit power increases by the square root of the number of uniformly weighted, defocused array elements [15], [20], [22]. For 3-D imaging using an N element linear array with each element consisting of M defocused elements aligned in the direction normal to the linear array, the transmit power is proportional to $N\sqrt{M}$. In the limiting case, an $N \times N$ 2-D array can be configured as a single N -element horizontal linear array by defocusing N -elements on each column, and the transmit power of this array becomes proportional to $N\sqrt{N}$. Similarly, a diagonal defocused linear

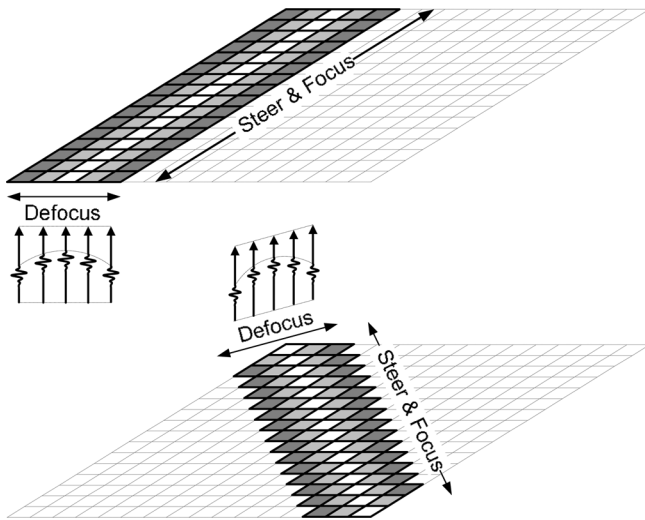


Fig. 11. Forming linear vertical (top) and diagonal (bottom) arrays using electronic defocusing.

array on an $N \times N$ array can also be formed where each virtual element consists of a different number of defocused elements which corresponds to a triangular apodization across the diagonal linear array. Such array reconfigurations can be applied directly to the proposed techniques here to improve the transmit power. Reconfiguring the array in transmit and receive and/or in different firings, called as reconfigurable array design, has been used in 3-D imaging for improving frame rate and/or reducing the array front-end complexity [7], [49], [51]. In general, the XT-FR produces the best image quality and involves the largest receive channel count when compared to XT-BR, XT-PR, and BRT-BCR. The front-end complexities of the XT-BR, XT-PR, and BRT-BCR are very similar, while the image quality of the XT-BR is better than the other two. The realization of aperture apodization for a given minimum f-number and/or for suppression of side lobe levels is straightforward for XT-FR and XT-PR, and XT-BR in transmit, whereas the apodization for BRT-BCR and receive apodization for XT-BR can be realized using multiple acquisitions with different weighting kernels [13], [56].

IV. SUMMARY AND CONCLUSION

We explored reduced redundancy array configurations for miniature volumetric imaging systems. Each configuration forms a coarray that captures all the spatial frequency content with a reduced number of active channels and firing count, and possesses a different tradeoff between image quality and front-end complexity. We explored fan-beam processing to reduce the number of firings in real-time volumetric scanning. We presented theoretical and simulated PSFs of the array configurations along with quantitative comparison in terms of the front-end complexity and image quality.

Coarray design aims to reduce the active element count while maintaining the image quality of the fully populated array. This is achieved by eliminating the transmit–receive element combinations producing redundant spatial frequencies. For an $N \times N$ -element transducer array, the kernel coarray (with no redundancy) is the fully filled $(2N - 1) \times (2N - 1)$ -element array, where each of its elements is formed by only a

single transmit–receive element combination. Additionally, the weighting of each coarray element must be adjustable independently by the transmit and receive element weights in the firing scenario. This allows controlling the PSF shape, the main and side-lobe levels; otherwise the resulting PSF cannot be matched to that of the fully populated array. The array configurations explored in this study produce coarrays with controllable main and side lobe levels via aperture apodization. This leads to considering forming larger arrays using the explored configurations instead of forming relatively smaller fully populated arrays for a given channel count. In addition, the array configurations presented here can also be used together with most of the existing array processing techniques such as subarray micro-beamforming and coded-excitation. Moreover, the explored array configurations are scalable to larger arrays by using larger transducer arrays or by forming larger arrays using small modular subarrays.

Depending on the back-end hardware requirements, the transmit and receive arrays in any array configuration can be interchanged while producing the same coarray function and PSF. For example, such re-configuration of XT-FR and XT-BR, improves the image SNR, and simplicity of the receive front-end, but reduces the frame rate and increases the transmit front-end complexity. We aim to use the XT-FR and XT-BR array configurations for endoscopic imaging. We have already implemented a custom front-end IC for real-time imaging using a 16×16 CMUT array, and demonstrated successful results [9], [54]. Currently we are working on implementation of a new custom, programmable front-end IC chip which can be used to realize any of the array designs discussed here [55]. Our future studies will focus on testing of the array configurations using experimental setups based on our custom front-end IC chips and 2-D CMUT arrays.

REFERENCES

- [1] A. Fenster, D. B. Downey, and H. N. Cardinal, "Three dimensional ultrasound imaging," *Phys. Med. Biol.*, vol. 46, pp. R67–R69, May 2001, 99.
- [2] R. C. Houck, J. Cooke, and E. A. Gill, "Three-Dimensional echo: Transition from theory to real-time, a technology now ready for prime time," *Curr. Problems Diagnostic Radiol.*, vol. 34, no. 3, pp. 85–105, 2005.
- [3] R. M. Lang, V. Mor-Avi, L. Sugeng, P. S. Nieman, and D. J. Sahn, "Three dimensional echocardiography: The benefits of the additional dimension," *J. Amer. College Cardiol.*, vol. 48, no. 10, pp. 2053–2069, 2006.
- [4] R. C. Houck, J. E. Cooke, and E. A. Gill, "Live 3D echocardiography: A replacement for traditional 2D echocardiography?," *Amer. J. Roentgenol.*, vol. 187, no. 4, pp. 1092–1106, Oct. 2006.
- [5] E. A. Gill and B. Klas, "Three-dimensional echocardiography: An historical perspective," *Cardiol. Clinics*, vol. 25, no. 2, pp. 221–229, May 2007.
- [6] I. S. Salgo, "Three-dimensional echocardiographic technology," *Cardiol. Clinics*, vol. 25, no. 2, pp. 231–239, May 2007.
- [7] B. Savord and R. Solomon, "Fully sampled matrix transducer for real time 3D ultrasonic imaging," in *IEEE Ultrason. Symp.*, Oct. 2003, pp. 945–953.
- [8] O. Oralkan, A. S. Ergun, J. A. Johnson, M. Karaman, and B. T. Khuri-Yakub, "Volumetric acoustic imaging using two-dimensional capacitive micromachined transducer arrays," *IEEE Trans. Ultrason., Ferroelectr., Freq. Control*, vol. 50, no. 11, pp. 1581–1594, Nov. 2003.
- [9] I. O. Wygant, X. Zhuang, D. T. Yeh, S. Vaithilingam, A. Nikoozadeh, O. Oralkan, A. S. Ergun, M. Karaman, and B. T. Khuri-Yakub, "An endoscopic imaging system based on a two-dimensional cMUT array: Real-time imaging results," in *Proc. IEEE Ultrason. Symp.*, Sep. 2005, vol. 2, pp. 792–795.
- [10] K. E. Thomenius, "Evolution of ultrasound beamformers," in *Proc. IEEE Ultrason. Symp.*, Nov. 1996, vol. 2, pp. 1615–1622.

- [11] E. Brunner, "How ultrasound system considerations influence front-end component choice," *Analog Dialogue*, vol. 36, no. 3, pp. 1–4, May–Jul. 2002.
- [12] L. F. Nock and G. E. Trahey, "Synthetic receive aperture imaging with phase correction for motion and for tissue inhomogeneities. I. Basic principles," *IEEE Trans. Ultrason., Ferroelect., Freq. Contr.*, vol. 39, no. 4, pp. 489–495, Jul. 1992.
- [13] R. J. Kozick and S. A. Kassam, "Synthetic aperture pulse-echo imaging with rectangular boundary arrays," *IEEE Trans. Image Process.*, vol. 2, no. 1, pp. 68–79, Jan. 1993.
- [14] J. T. Ylitalo and H. Ermert, "Ultrasound synthetic aperture imaging: Monostatic approach," *IEEE Trans. Ultrason., Ferroelect., Freq. Contr.*, vol. 41, no. 3, pp. 333–339, May 1994.
- [15] M. Karaman, P. C. Li, and M. O'Donnell, "Synthetic aperture imaging for small scale imaging systems," *IEEE Trans. Ultrason. Ferroelect. Freq. Contr.*, vol. 42, no. 3, pp. 429–442, May 1995.
- [16] R. Y. Chiao and L. J. Thomas, "Aperture formation on reduced-channel arrays using the transmit-receive apodization matrix," in *Proc. IEEE Ultrason. Symp.*, Nov. 1996, vol. 2, pp. 1567–1571.
- [17] M. O'Donnell, M. J. Eberle, D. N. Stephens, J. L. Litza, K. San Vicente, and B. M. Shapo, "Synthetic phased arrays for intraluminal imaging of coronary arteries," *IEEE Trans. Ultrason., Ferroelect., Freq. Contr.*, vol. 44, no. 3, pp. 714–721, May 1997.
- [18] M. Karaman, H. S. Bilge, and M. O'Donnell, "Adaptive multielement synthetic aperture imaging with motion and phase aberration correction," *IEEE Trans. Ultrason., Ferroelect., Freq. Contr.*, vol. 45, no. 4, pp. 1077–1087, Jul. 1998.
- [19] G. R. Lockwood, J. R. Talman, and S. S. Brunke, "Real-time 3-D ultrasound imaging using sparse synthetic aperture beamforming," *IEEE Trans. Ultrason., Ferroelect., Freq. Contr.*, vol. 45, no. 4, pp. 980–988, Jul. 1998.
- [20] C. H. Frazier and W. D. O'Brien, "Synthetic aperture techniques with a virtual source element," *IEEE Trans. Ultrason., Ferroelect., Freq. Contr.*, vol. 45, no. 1, pp. 196–207, Jan., 1998.
- [21] C. R. Hazard and G. R. Lockwood, "Effects of motion on a synthetic aperture beamformer for real-time 3D ultrasound," in *Proc. IEEE Ultrason. Symp.*, 1999, vol. 2, pp. 1221–1224.
- [22] S. I. Nikolov and J. A. Jensen, "3D synthetic aperture imaging using a virtual source element in the elevation plane," in *Proc. IEEE Ultrason. Symp.*, 2000, pp. 1743–1747.
- [23] K. L. Gammelmark and J. A. Jensen, "Multielement synthetic transmit aperture imaging using temporal encoding," *IEEE Trans. Med. Imag.*, vol. 22, no. 4, pp. 552–563, Apr. 2003.
- [24] K.-S. Kim and T.-K. Song, "High volume rate 3D ultrasound imaging using cross array based on synthetic transmit focusing," in *Proc. IEEE Ultrason. Symp.*, Aug. 2004, vol. 2, pp. 1409–1412.
- [25] R. E. Davidsen, J. A. Jensen, and S. W. Smith, "Two-dimensional random arrays for real-time volumetric imaging," *Ultrason. Imag.*, vol. 16, pp. 143–163, 1994.
- [26] G. R. Lockwood and F. S. Foster, "Optimising the radiation pattern of sparse periodic two-dimensional arrays," *IEEE Trans. Ultrason., Ferroelect., Freq. Contr.*, vol. 43, no. 1, pp. 15–19, Jan. 1996.
- [27] J. L. Schwartz and B. D. Steinberg, "Ultrasparse, ultrawideband arrays," *IEEE Trans. Ultrason., Ferroelect., Freq. Contr.*, vol. 45, no. 2, pp. 376–393, Mar. 1998.
- [28] S. I. Nikolov and J. A. Jensen, "Application of different spatial sampling patterns for sparse array transducer design," *Ultrasonics*, vol. 37, no. 10, pp. 667–671, 2000.
- [29] J. T. Yen, J. P. Steinberg, and S. W. Smith, "Sparse 2-D array design for real time rectilinear volumetric imaging," *IEEE Trans. Ultrason., Ferroelect., Freq. Contr.*, vol. 47, no. 1, pp. 93–110, Jan. 2000.
- [30] A. Austeng and S. Holm, "Sparse 2-D arrays for 3-D phased array imaging—Design methods," *IEEE Trans. Ultrason., Ferroelect., Freq. Contr.*, vol. 49, no. 8, pp. 1073–1086, Aug. 2002.
- [31] S. W. Smith, H. G. Pavy, Jr., and O. T. von Ramm, "High speed ultrasound volumetric imaging system—Part I. Transducer design and beam steering," *IEEE Trans. Ultrason., Ferroelect., Freq. Contr.*, vol. 38, no. 2, pp. 100–108, Mar. 1991.
- [32] O. T. von Ramm, S. W. Smith, and H. Puly, "High-speed ultrasound volumetric imaging systems—Part II: Parallel processing and image display," *IEEE Trans. Ultrason., Ferroelect., Freq. Contr.*, vol. 38, no. 2, pp. 109–115, Mar. 1991.
- [33] A. Drukarev, K. Konstantinides, and G. Seroussi, "Beam transformation techniques for ultrasonic medical imaging," *IEEE Trans. Ultrason., Ferroelect., Freq. Contr.*, vol. 40, no. 6, pp. 717–725, Nov. 1993.
- [34] K. Wall and G. R. Lockwood, "A new multi-beam approach to real-time 3D imaging," in *Proc. IEEE Ultrason. Symp.*, Oct. 2002, pp. 1759–1762.
- [35] J. Cheng and J.-Y. Lu, "Extended high-frame rate imaging method with limited-diffraction beams," *IEEE Trans. Ultrason., Ferroelect., Freq. Contr.*, vol. 53, no. 5, pp. 880–899, May 2006.
- [36] T. Hergum, T. Bjustad, K. Kristoffersen, and H. Torp, "Parallel beamforming using synthetic transmit beams," *IEEE Trans. Ultrason., Ferroelect., Freq. Contr.*, vol. 54, no. 2, pp. 271–280, Feb. 2007.
- [37] J. T. Yen and S. W. Smith, "Real-time rectilinear volumetric imaging," *IEEE Trans. Ultrason., Ferroelect., Freq. Contr.*, vol. 49, no. 1, pp. 114–124, Jan. 2002.
- [38] J. T. Yen and S. W. Smith, "Real-time rectilinear 3-D ultrasound using receive mode multiplexing," *IEEE Trans. Ultrason., Ferroelect., Freq. Contr.*, vol. 51, no. 2, pp. 216–226, Feb. 2004.
- [39] N. M. Daher and J. T. Yen, "2D array for 3D ultrasound imaging using synthetic aperture techniques," *IEEE Trans. Ultrason., Ferroelect., Freq. Contr.*, vol. 53, no. 5, pp. 912–924, May 2006.
- [40] M. Karaman and M. O'Donnell, "Subaperture processing for ultrasound imaging," *IEEE Trans. Ultrason. Ferroelect. Freq. Contr.*, vol. 45, no. 1, pp. 1–10, Jan. 1998.
- [41] J. A. Johnson, M. Karaman, and B. T. Khuri-Yakub, "Coherent array imaging using phased subarrays—Part I: Basic principles," *IEEE Trans. Ultrason., Ferroelect., Freq. Contr.*, vol. 52, no. 1, pp. 37–50, Jan. 2005.
- [42] J. A. Johnson, O. Oralkan, A. S. Ergun, U. Demirci, M. Karaman, and B. T. Khuri-Yakub, "Coherent array imaging using phased subarrays—Part II: Simulation and experimental results," *IEEE Trans. Ultrason., Ferroelect., Freq. Contr.*, vol. 52, no. 1, pp. 51–64, Jan. 2005.
- [43] T. Misaridis and P. Munk, "High frame rate imaging using parallel transmission of focused coded fields," in *Proc. IEEE Ultrason. Symp.*, 2000, vol. 2, pp. 1417–1420.
- [44] M.-H. Bae, W.-Y. Lee., M.-K. Jeong, and S.-J. Kwon, "Orthogonal golay code based ultrasonic imaging without reducing frame rate," in *Proc. IEEE Ultrason. Symp.*, Oct. 2002, vol. 2, pp. 1705–1708.
- [45] R. Y. Chiao and X. Hao, "Coded excitation for diagnostic ultrasound: A system developer's perspective," *IEEE Trans. Ultrason., Ferroelect., Freq. Contr.*, vol. 52, no. 2, pp. 160–170, Feb. 2005.
- [46] M. O'Donnell and Y. Wang, "Coded excitation for synthetic aperture ultrasound imaging," *IEEE Trans. Ultrason., Ferroelect., Freq. Contr.*, vol. 52, no. 2, pp. 171–176, Feb. 2005.
- [47] B. Savord, "Phased array acoustic systems with inter-group processors," U.S. Patent 5 997 479.
- [48] B. Savord, "Beamforming methods and apparatus for three-dimensional ultrasound imaging using two-dimensional transducer array," U.S. Patent 6 013 032.
- [49] R. Fisher, R. Wodnicki, S. Cogan, R. Thomas, D. Mills, C. Woychik, R. Lewandowski, and K. Thomenius, "Packaging and design of reconfigurable arrays for volumetric imaging," in *Proc. IEEE Ultrason. Symp.*, Oct. 2007, pp. 407–410.
- [50] C. M. W. Daft, D.-L. D. Liu, P. A. Wagner, and I. Ladabaum, "Multi-dimensional CMUT array with integrated beamformation," U.S. Patent Application 20070242567.
- [51] C. Daft, D. Brueske, P. Wagner, and D. Liu, "A matrix transducer design with improved image quality and acquisition rate," in *Proc. IEEE Ultrason. Symp.*, Oct., 2007, pp. 411–415.
- [52] T. L. Proulx, C. M. Daft, Mohr, J. Paul, T. W. Wilser, C. E. Bradley, P. A. Wagner, and I. Ladabaum, "Ultrasound imaging transducer array for synthetic aperture," U.S. Patent Application 20070167752.
- [53] A. Savoia, V. Bavaro, G. Caliano, A. Caronti, R. Carotenuto, P. Gatta, C. Longo, and M. Pappalardo, "Crisscross 2D cMUT array: Beamforming strategy and synthetic 3D imaging results," in *Proc. IEEE Ultrason. Symp.*, Oct. 2007, pp. 1514–1517.
- [54] I. O. Wygant, X. Zhuang, D. T. Yeh, O. Oralkan, A. S. Ergun, M. Karaman, and B. T. Khuri-Yakub, "Integration of 2D CMUT arrays with front-end electronics for volumetric ultrasound imaging," *IEEE Trans. Ultrason., Ferroelect., Freq. Contr.*, vol. 55, no. 2, pp. 327–342, Feb. 2008.
- [55] I. O. Wygant, H. J. Lee, A. Nikoozadeh, Ö. Oralkan, M. Karaman, and B. T. Khuri-Yakub, "An integrated circuit with transmit beamforming and parallel receive channels for real-time three-dimensional ultrasound imaging," in *Proc. IEEE Ultrason. Symp.*, Oct. 2006, pp. 2186–2189.
- [56] R. T. Hocter and S. A. Kassam, "The unifying role of the coarray in aperture synthesis for coherent and incoherent imaging," *Proc. IEEE*, vol. 78, no. 4, pp. 735–752, Apr. 1990.
- [57] A. R. Selfridge, G. S. Kino, and B. T. Khuri-Yakub, "A theory for the radiation pattern of a narrow strip acoustic transducer," *Appl. Phys. Lett.*, vol. 37, no. 1, pp. 35–36, Jul. 1980.
- [58] C. E. Bradley, C. M. Daft, I. Ladabaum, J. P. Mohr III, T. Proulx, P. A. Wagner, and W. T. Wilser, "Ultrasound imaging transducer array for synthetic aperture," EPO Patent Application EP 1 795 917 A2.